Elastic Least-Squares Reverse-Time Migration Based on a Modified Acoustic-Elastic Coupled Equation for OBS Four-Component Data

Minao Sun, Shuanggen Jin, and Pengfei Yu, *Member, IEEE*

***Abstract*— Elastic least-squares reverse-time migration (ELSRTM) yields subsurface high-resolution elastic images from multicomponent seismic data. For ocean bottom seismic (OBS) acquisitions, both pressure and displacement components are measured using four-component (4C) modern receivers. However, these 4C data cannot be effectively simulated and migrated using conventional ELSRTM approaches due to the limitation of the standard elastic wave equation. For this reason, we propose a new ELSRTM method based on a modified acoustic-elastic coupled (AEC) equation. Owing to this equation, either the prediction or the migration of OBS 4C data can be implemented using a one-time wavefield simulation. Incorporation with a perturbation imaging condition, the proposed method can invert for P- and S-wave velocity and density and generate amplitude-preserving images. Besides, it can provide subsurface impedance reflectivity models by stacking the obtained multi-parameter images. In the least-squares migration, a preconditioned conjugate gradient algorithm is implemented based on a multi-parameter diagonal Hessian. Numerical experiments on an uncorrelated layer model and a portion of the Southern Yellow China sea model can demonstrate the effectiveness of this method on improving imaging resolution and accelerating convergence rate.**

***Index Terms*— Least-squares migration (LSM), multicomponent, multiparameter, ocean bottom seismic (OBS) data, reverse-time migration.**

I. Introduction

REVERSE time migration (RTM) is a powerful tool to reveal Earth's interior from observed seismic data. By solving the two-way acoustic wave equation, RTM can overcome the energy evanescence in the ray-based approaches [1], [2]. However, the observed data always suffer from limited recording aperture, narrow frequency bandwidth, and irregular source–receiver distributions. As a result, RTM results in degraded images with imprecise amplitude and unsatisfied imaging resolution [3]. Least-squares migration (LSM) formulates the classical migration as a linear inverse problem and seeks optimal images that can best match observed data [4]. Compared with RTM, least-squares RTM (LSRTM) can improve the resolution and suppress migration artifacts [5]–[13]. Nowadays, it has been developed to consider more physical parameters [14], [15] and high-order multiples [16].

With the rapid development of OBS acquisitions in deep-sea resource explorations, elastic wave phenomena, i.e., wave-mode conventions and amplitude variation versus offset effects, become increasingly significant in far-offset observed data. Consequently, acoustic approaches may lead to false interfaces and migration artifacts in obtained images [17]. As governed by the elastic wave equation, elastic RTM (ERTM) can interpret complicated wave phenomena and yield subsurface images associated with P- and S-waves [18]–[21]. The recovered elastic profiles can be used to validate bright-spot reflections, estimate the Poisson's ratio, and detect fractures through shear-wave splitting for anisotropic media [22]. For elastic LSRTM (ELSRTM), Stanton and Sacchi [23], [24] use an explicit one-way migration operator to implement the elastic LSM and combine a P- and S-wave separation to give high-resolution *PP* and *PS* images. Besides, the ELSRTM method based on the two-way equation can automatically correct the polarity reversals and mitigate the parameter coupling effects [25]–[28]. With consideration of the density variation, a density-variable ELSRTM approach has been proved to enhance the amplitude fidelity and estimate impedance reflectivity model [29], [30].

By locating 4C receivers on the seabed, ocean bottom seismometer measures one pressure and three displacement components. However, the standard elastic wave equation in ELSRTM cannot directly predict nor utilize these components. Many geophysicists proposed a fluid-solid coupled equation to solve the acoustic and elastic wave equations in different computing areas, respectively [31]–[34]. This strategy allows one to compute the pressure wavefield in the water immediately above the seabed and the displacement wavefields on the solid seabed, but it requires to explicitly implement the correct boundary conditions on the seabed [35]. Furthermore,

Manuscript received May 15, 2020; revised September 22, 2020, November 12, 2020, and December 16, 2020; accepted December 20, 2020. Date of publication January 14, 2021; date of current version October 26, 2021. This work was supported in part by the China Postdoctoral Science Foundation under Grant 2020M671539; in part by the National Key Research and Development Program of China Project under Grant 2018YFC0603502 and Grant 2018YFC0310100; and in part by the National Natural Science Foundation of China under Grant 41930105 and Grant 42074149. *(Corresponding authors: Shuanggen Jin; Pengfei Yu.)*

Minao Sun is with the School of Remote Sensing and Geomatics Engineering, Nanjing University of Information Science and Technology, Nanjing 210044, China (e-mail: minaosun@nuist.edu.cn).

Shuanggen Jin is with the School of Remote Sensing and Geomatics Engineering, Nanjing University of Information Science and Technology, Nanjing 210044, China, and also with the Key Laboratory of Planetary Sciences, Shanghai Astronomical Observatory, Chinese Academy of Sciences, Shanghai 200030, China (e-mail: sgjin@shao.ac.cn).

Pengfei Yu is with the College of Oceanography, Hohai University, Nanjing 210098, China (e-mail: hhu_ypf@hhu.edu.cn).

Digital Object Identifier 10.1109/TGRS.2020.3047117

it becomes more challenging for the media with surface topography and irregular interfaces [36]–[38]. Alternatively, Yu *et al.* [39] introduced the relationship between the pressure and the normal stress components into the elastic wave equation. The obtained acoustic-elastic coupled (AEC) equation uses one more formula to extract the pressure component from elastic wavefields instead of performing a *P*/*S* wavefield decomposition. Because this AEC equation can be applied in both fluid and solid areas, there is no need to implement the boundary conditions. The developed ERTM approach for OBS 4C data shows to suppress the non-physical migration artifacts effectively and has been further extended to combine the vector imaging condition [40] and consider anisotropic properties [41].

This study develops a new ELSRTM method based on a modified AEC equation (AEC-LSRTM). The modifications on the original AEC equation allow one to predict and migrate the 4C seismic data but reduce memory requirement. This method defines a new misfit function for OBS 4C data to adjust the weights of displacement and pressure components. Incorporation with the perturbation imaging condition, it can simultaneously invert for *P*- and *S*-wave velocities and density and thus provide quantitative estimations of impedance reflectivity. To accelerate the convergence rate, the LSM is implemented using a preconditioned conjugate-gradient algorithm with a multi-parameter diagonal Hessian. This article is organized as follows. Section II introduces the methodology of this AEC-LSRTM method and summarizes the detailed implementation of LSM. In Section III, we use two numerical examples to validate the effectiveness and accuracy of the proposed AEC-LSRTM method with a comparison of ELSRTM. Before conclusions, we investigate the potential of this method for joint imaging of sparse OBN and marine towed-streamer data.

II. Methodology

A. ERTM Based on the Modified AEC Equation

The modified 2-D displacement-stress AEC equation can generate OBS 4C data, given by (for details see Appendix A)

$$\begin{cases} \rho\dfrac{\partial^2 u_x}{\partial t^2}-\dfrac{\partial\left(\tau_n^s-p\right)}{\partial x}-\dfrac{\partial\tau_s^s}{\partial z}=0 \\ \rho\dfrac{\partial^2 u_z}{\partial t^2}-\dfrac{\partial\tau_s^s}{\partial x}-\dfrac{\partial\left(-\tau_n^s-p\right)}{\partial z}=0 \\ p+(\lambda+\mu)\left(\dfrac{\partial u_x}{\partial x}+\dfrac{\partial u_z}{\partial z}\right)=f_p \\ \tau_n^s-\mu\left(\dfrac{\partial u_x}{\partial x}-\dfrac{\partial u_z}{\partial z}\right)=0 \\ \tau_s^s-\mu\left(\dfrac{\partial u_x}{\partial z}+\dfrac{\partial u_z}{\partial x}\right)=0 \end{cases} \tag{1}$$

where p indicates the pressure component of the elastic wavefield, u_x and u_z denote the horizontal- and vertical-particle displacement components, and τ_s^s and τ_n^s are the defined deviatoric stress components related to *S*-wave. λ and μ are the Lamé constants, and ρ is density. f_p indicates the source function to yield a pure *P*-wave. Because the modified AEC equation is solved in both fluid and solid areas, there is no need to implement the boundary conditions even for irregular grids and surface topography.

Based on the classical migration theory, seismic data $\mathbf{d}$ can be predicted using a linear Born modeling

$$\mathbf{d}=\mathbf{L}\mathbf{m}_{\text{ref}}. \tag{2}$$

where $\mathbf{L}$ is the Born operator and $\mathbf{m}_{\text{ref}}$ indicates the reflectivity model. The elastic Born modeling equation for OBS 4C data can be derived by dividing the parameters and the wavefields into background and perturbed parts

$$\begin{cases} \rho\dfrac{\partial^2\delta u_x}{\partial t^2}-\dfrac{\partial\left(\delta\tau_n^s-\delta p\right)}{\partial x}-\dfrac{\partial\delta\tau_s^s}{\partial z}=-\delta\rho\dfrac{\partial^2 u_x}{\partial t^2} \\ \rho\dfrac{\partial^2\delta u_z}{\partial t^2}+\dfrac{\partial\delta\tau_s^s}{\partial x}-\dfrac{\partial\left(-\delta\tau_n^s-\delta p\right)}{\partial z}=-\delta\rho\dfrac{\partial^2 u_z}{\partial t^2} \\ \delta p+(\lambda+\mu)\left(\dfrac{\partial\delta u_x}{\partial x}+\dfrac{\partial\delta u_z}{\partial z}\right)=-(\delta\lambda+\delta\mu)\left(\dfrac{\partial u_x}{\partial x}+\dfrac{\partial u_z}{\partial z}\right) \\ \delta\tau_n^s-\mu\left(\dfrac{\partial\delta u_x}{\partial x}-\dfrac{\partial\delta u_z}{\partial z}\right)=\delta\mu\left(\dfrac{\partial u_x}{\partial x}-\dfrac{\partial u_z}{\partial z}\right) \\ \delta\tau_s^s-\mu\left(\dfrac{\partial\delta u_x}{\partial z}+\dfrac{\partial\delta u_z}{\partial x}\right)=\delta\mu\left(\dfrac{\partial u_x}{\partial z}+\dfrac{\partial u_z}{\partial x}\right). \end{cases} \tag{3}$$

To simultaneously make use of observed pressure and displacement components, a weighted misfit function for OBS 4C data $E(\mathbf{m})$ is adopted, given by

$$E(\mathbf{m})=\frac{1}{2}\varepsilon\cdot\|\delta\mathbf{d}_u\|^2+\frac{1}{2}(1-\varepsilon)\cdot\zeta\cdot\left\|\delta d_p\right\|^2 \tag{4}$$

where $\delta\mathbf{d}_u$ and δd_p denote the data residuals of the displacement and pressure components, respectively. Here, ε is a weighting coefficient, satisfying $\varepsilon\in[0,1]$, and a scale factor ζ is used to balance the difference in order of magnitude.

The migration image $\mathbf{m}_{\text{mig}}$ can be obtained by applying the adjoint Born operator $\mathbf{L}^T$ to the data residuals

$$\mathbf{m}_{\text{mig}}=\mathbf{L}^T\mathbf{f}'. \tag{5}$$

Substituting (2) into (5), the adjoint modified AEC equation satisfies (details see Appendix B)

$$\begin{cases} \rho\dfrac{\partial^2\hat{u}_x}{\partial t^2}-\dfrac{\partial[(\lambda+\mu)\hat{p}]}{\partial x}+\dfrac{\partial\left[\mu\hat{\tau}_n^s\right]}{\partial x}+\dfrac{\partial\left[\mu\hat{\tau}_s^s\right]}{\partial z}=f'_x \\ \rho\dfrac{\partial^2\hat{u}_z}{\partial t^2}-\dfrac{\partial[(\lambda+\mu)\hat{p}]}{\partial z}-\dfrac{\partial\left[\mu\hat{\tau}_n^s\right]}{\partial z}+\dfrac{\partial\left[\mu\hat{\tau}_s^s\right]}{\partial x}=f'_z \\ \hat{p}-\left(\dfrac{\partial\hat{u}_x}{\partial x}+\dfrac{\partial\hat{u}_z}{\partial z}\right)=f'_p \\ \hat{\tau}_n^s+\left(\dfrac{\partial\hat{u}_x}{\partial x}-\dfrac{\partial\hat{u}_z}{\partial z}\right)=0 \\ \hat{\tau}_s^s+\left(\dfrac{\partial\hat{u}_x}{\partial z}+\dfrac{\partial\hat{u}_z}{\partial x}\right)=0 \end{cases} \tag{6}$$

where $\left(\hat{u}_x,\hat{u}_z,\hat{p},\hat{\tau}_n^s,\hat{\tau}_s^s\right)$ is the adjoint wavefields of $\left(u_x,u_z,p,\tau_n^s,\tau_s^s\right)$, and $\left(f'_x,f'_z,f'_p\right)$ is the multicomponent adjoint sources

$$\begin{bmatrix} f'_x \\ f'_z \\ f'_p \end{bmatrix}=\begin{bmatrix} \varepsilon\cdot\delta d_x \\ \varepsilon\cdot\delta d_z \\ (1-\varepsilon)\cdot\zeta\cdot\delta d_p \end{bmatrix}. \tag{7}$$

Since the 4C data residuals are injected into the backpropagated wavefields, both pressure and displacement components can contribute to multiparameter images.

The perturbations of Lamé constants and density (λ, μ, ρ) can be estimated by computing the zero-lag cross correlation between the adjoint wavefields and the forward wavefields, given by

$$\begin{aligned}\delta\lambda &= -\frac{p}{\lambda+\mu}\hat{p}\\ \delta\mu &= -\frac{p}{\lambda+\mu}\hat{p} - \frac{\tau_n^s}{\mu}\hat{\tau}_n^s - \frac{\tau_s^s}{\mu}\hat{\tau}_s^s\\ \delta\rho &= \frac{\partial^2 u_x}{\partial t^2}\hat{u}_x + \frac{\partial^2 u_z}{\partial t^2}\hat{u}_z.\end{aligned} \tag{8}$$

According to the chain rule, the perturbations of P-wave velocity, S-wave velocity, and density (Vp, Vs, ρ) can be computed

$$\begin{aligned}\delta Vp &= 2\rho Vp^2 \cdot \delta\lambda\\ \delta Vs &= -4\rho Vs^2 \cdot \delta\lambda + 2\rho Vs^2 \cdot \delta\mu\\ \delta\rho_{vel} &= \rho\left(Vp^2 - 2Vs^2\right)\cdot\delta\lambda + \rho Vs^2\cdot\delta\mu + \rho\delta\rho.\end{aligned} \tag{9}$$

To eliminate the dimension differences in order of magnitude for different parameter classes, the reflectivity model is defined as the relative parameter perturbation $\mathbf{m}_{\text{mig}} = \delta\mathbf{m}/\mathbf{m}$.

B. Implementation of Least-Squares Migration

By formulating a least-squares linear inverse problem, the optimal images can be sought when the minimum is attained, the reflectivity model $\mathbf{m}_{\text{ref}}$ can be obtained as the solution of the Newton normal equation

$$\mathbf{m}_{\text{mig}} = \left(\mathbf{L}^T\mathbf{L}\right)\mathbf{m}_{\text{ref}}. \tag{10}$$

Here, $\mathbf{L}^T\mathbf{L}$ is the Hessian operator, which is the second-order partial derivative of the misfit function (4) with respect to parameters. In this study, the multi-parameter Hessian is a 3×3 block matrix associated with P- and S-wave velocities and density. The diagonal blocks of the Hessian are formed by the correlations of the sensitivity kernels of the same parameter class, reflecting the data bandwidth and the observation aperture. The non-diagonal blocks describe the internal couplings between different parameter classes. The accuracy of the Hessian operator has a great influence on the inverted reflectivity model. Therefore, well-resolved subsurface images can be obtained only if correct Hessian operator is utilized.

In this method, the LSM is implemented using a preconditioned conjugate gradient (PCG) loop as shown in Algorithm 1. To improve the convergence rate, a multi-parameter diagonal Hessian has been used, which is derived based on the modified AEC equation (see details in Appendix C). In each iteration, the demigration $\mathbf{L}\mathbf{p}_k$ and the migration $\mathbf{L}^T(\mathbf{L}\mathbf{p}_k)$ processes for OBS 4C data are implemented according to (2) and (6), respectively. When the PCG loop is finished, the LSM images of P- and S-wave velocities and density can be obtained.

Compared with the velocity perturbations, the contrasts of elastic impedance can better represent reflecting the characters of subsurface structures. In vertical incident cases, the elastic impedance satisfies $Ip = \rho Vp$ and $Is = \rho Vs$. Thus, we can get

$$\begin{aligned}\frac{\delta Ip}{Ip} &= \frac{\delta Vp}{Vp} + \frac{\delta\rho}{\rho}\\ \frac{\delta Is}{Is} &= \frac{\delta Vs}{Vs} + \frac{\delta\rho}{\rho}.\end{aligned} \tag{11}$$

It shows that the relative perturbations of elastic impedance can be easily computed by stacking the recovered images of P-/S-wave velocities and density, given by

$$\begin{aligned}Ip_{\text{ref}} &= Vp_{\text{ref}} + \rho_{\text{ref}}\\ Is_{\text{ref}} &= Vs_{\text{ref}} + \rho_{\text{ref}}.\end{aligned} \tag{12}$$

The workflow of the proposed AEC-LSRTM method is shown in Fig. 1. In the first step, we need to generate the forward wavefields excited by a pure P-wave source and the adjoint wavefields backpropagated with 4C data residuals. By applying the imaging conditions to these wavefields, we can obtain the multiparameter RTM images. Secondly, we implement the LSM using the PCG loop, including multiple-time de-migration and migration processes. When the convergence condition is satisfied, we can obtain the final LSM images and estimate the impedance reflectivity models. Table I shows the computational comparison using different governing equations. Owing to the modifications on the original AEC equation, the proposed AEC-LSRTM method can simultaneously make use of OBS 4C data with similar computational costs as the conventional 3C ELSRTM method.

Algorithm 1 PCG Loop for LSM

Input: $\mathbf{m}_{mig}$, $\mathbf{H}_d$

Set $\mathbf{x}_0 = 0$ and $\mathbf{r}_0 = \left(\mathbf{L}^T\mathbf{L}\right)\mathbf{x}_0 - \mathbf{m}_{mig}$

Solve $\mathbf{H}_d\mathbf{y}_0 = \mathbf{r}_0$ for $\mathbf{y}_0$

Set $\mathbf{p}_0 = -\mathbf{r}_0$ and $k = 0$

Output: Estimated LSM images

while $\mathbf{r}_k \neq 0$ **do**
  $s_k = \frac{\mathbf{r}_k^T\mathbf{r}_k}{(\mathbf{L}\mathbf{p}_k)^T(\mathbf{L}\mathbf{p}_k)}$
  $\mathbf{x}_{k+1} = \mathbf{x}_k + s_k\mathbf{p}_k$
  $\mathbf{r}_{k+1} = \mathbf{r}_k + s_k\left[\mathbf{L}^T(\mathbf{L}\mathbf{p}_k)\right]$
  Solve $\mathbf{H}_d\mathbf{y}_{k+1} = \mathbf{r}_{k+1}$ for $\mathbf{y}_{k+1}$
  $t_{k+1} = \frac{\mathbf{r}_{k+1}^T\mathbf{y}_{k+1}}{\mathbf{r}_k^T\mathbf{y}_k}$
  $\mathbf{p}_{k+1} = -\mathbf{y}_{k+1} + t_{k+1}\mathbf{p}_k$
  $k = k + 1$
end while
return $\mathbf{x}_{k+1}$

III. Experimental Results

In this section, we use two numerical examples: 1) an uncorrelated layered model and 2) a portion of the Yellow China Sea model, to demonstrate the effectiveness of the AEC-LSRTM method for OBS 4C data. In these examples, an O(2, 8) time-space-domain finite-difference(FD) staggered-grid solution [42] of the modified AEC equation (1)

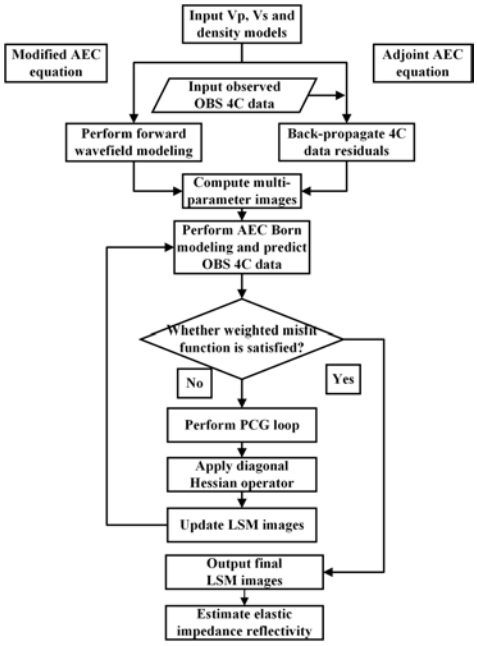

Fig. 1. Flowchat of the AEC-LSRTM method.

TABLE I
COMPUTATIONAL COMPARISON BETWEEN DIFFERENT GOVERNING EQUATIONS

Equation type	Standard elastic	Original AEC	Modified AEC
FD Times	8	8	8
Memory Cost	5	6	5
Data Fitting	3C	4C	4C

is used to generate both forward and back-propagated wavefields without consideration of a free-surface boundary condition. As a comparison, the conventional ELSRTM method is also performed using the same misfit function with only 3C displacement data.

A. Experiment 1: Uncorrelated Layered Model Test

The first experiment is tested on the uncorrelated layered model. The true models of *P*- and *S*-wave velocities and density are displayed in Fig. 2, and the migration ones are generated using a smoothing window of 30 m. The acquisition includes 61 sources below the sea surface and 301 OBS receivers on the seabed with sampling intervals of 50 and 10 m, respectively. A Ricker wavelet with a peak frequency of 20 Hz is adopted to generate a pure *P*-wave source. The total recording time is 3.0 s with a sampling rate of 1 ms. In the PCG loop of the LSM, the maximum iteration number is set to be 51.

Fig. 3 shows the migration images of Vp, Vs, and ρ. It is apparent that the shallow model is degraded by high-amplitude back-scatterings, and the deep layer shows unbalanced amplitude. It supports that the adjoint operator is not a good approximation for the inverse. Besides, the parameter couplings

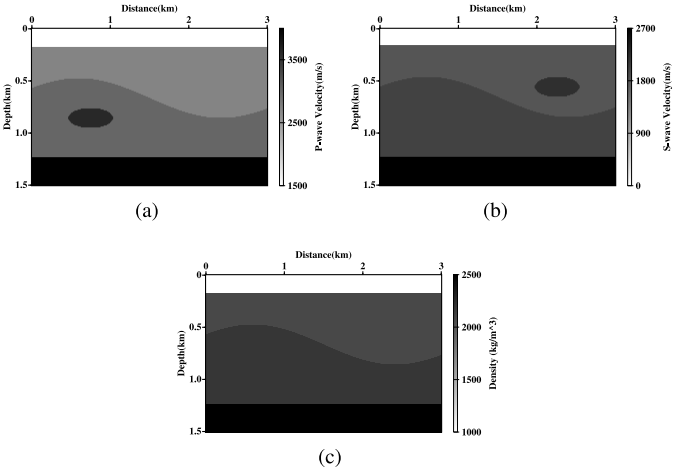

Fig. 2. True models of (a) Vp, (b) Vs, and (c) ρ.

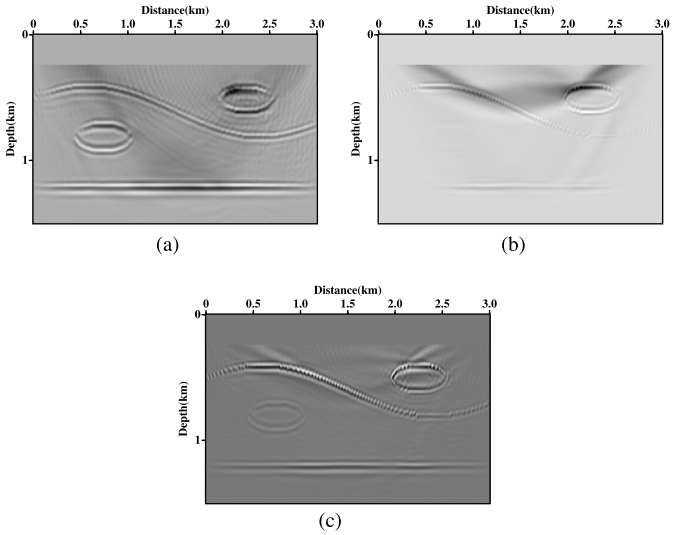

Fig. 3. Migration images of (a) Vp, (b) Vs, and (c) ρ using AEC-RTM.

cause some crosstalk footprints, which significantly reduce the quality of the images. Fig. 4 shows the final LSM images using AEC-LSRTM with OBS 4C data. After sufficient iterations, the images exhibit preserved amplitude, improved interface continuity, and suppressed footprints. It demonstrates that the AEC-LSRTM method can effectively remove the blurring effects of the Hessian and provide high-resolution parameter images.

The LSM images are also inverted using ELSRTM with 3C displacement data. As shown in Fig. 5, the coupling footprints are more serious, and the retrieved interfaces are more strongly distorted by artificial reflectors. Fig. 6 presents the vertical profiles of elastic impedance reflectivity models. The ELSRTM method overestimates the interfaces (see arrows in Fig. 6) and provides inaccurate reflectivity reconstructions with unexpected oscillations. In contrast, the AEC-LSRTM results (red lines) are much closer to the true ones (black lines) and have a higher resolution with narrower sidelobes.

Fig. 7 shows the single-shot data residuals of u_x- and u_z-components. In the AEC-LSRTM results, the amplitude of

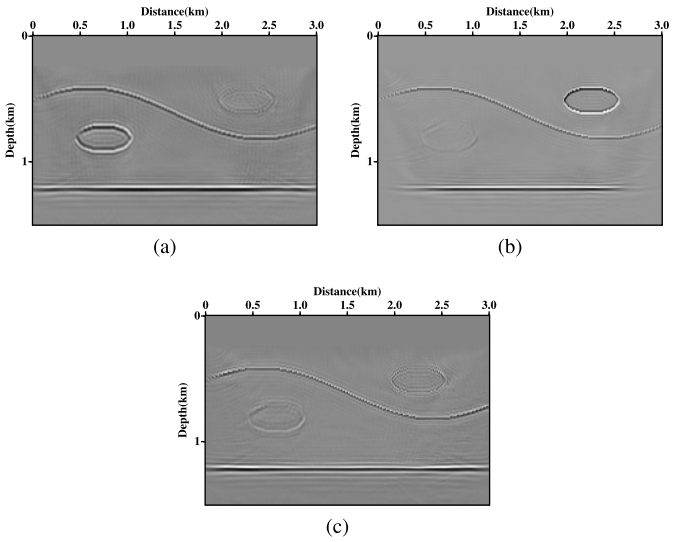

Fig. 4. Final LSM images of (a) Vp, (b) Vs, and (c) ρ using AEC-LSRTM.

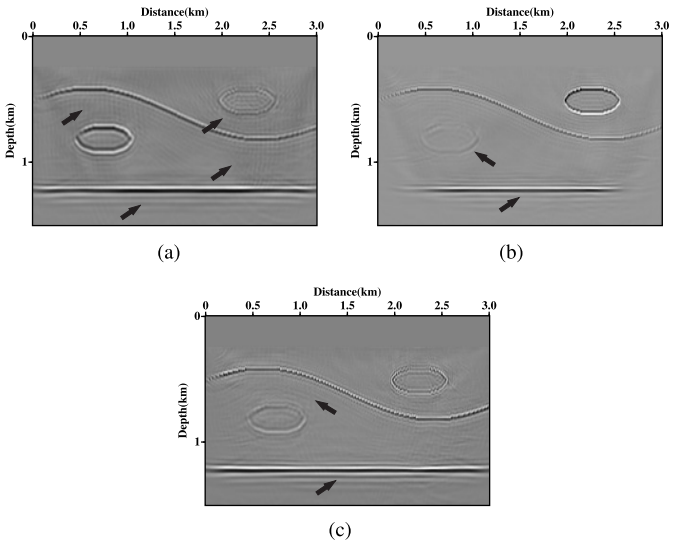

Fig. 5. Final LSM images of (a) Vp, (b) Vs, and (c) ρ using ELSRTM with only displacement data.

the data residuals is much weaker, which suggests that the AEC-LSRTM method can give more accurate interpretation of the observed data. Fig. 8 shows the normalized convergence profile of the weighted misfit function. As more data components are involved, AEC-LSRTM provides a higher convergence rate than ELSRTM and eventually converges to a lower misfit value.

B. Experiment 2: Southern Yellow Sea Model Test

The second experiment is performed on a portion of the Southern Yellow Sea model (see Fig. 9). The model is 8 km in width and 2.5 km in depth, which is re-sampled with 651 and 136 grids in horizontal and vertical directions, respectively. The migration models are generated using a smoothing window of 60 m. The acquisition includes 64 sources below the sea surface and 651 receivers on the seabed with intervals of 100 and 12.5 m, respectively. The total recording time is

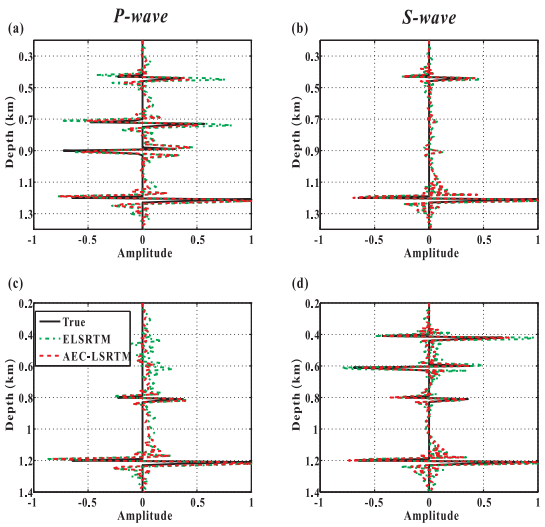

Fig. 6. Vertical profiles of P- and S-wave reflectivity models for true model (black solid lines), ELSRTM (green dotted lines), and AEC-LSRTM (red dashed lines) extracted at the horizontal distances of (Top) 0.75 km and (Bottom) 2.25 km.

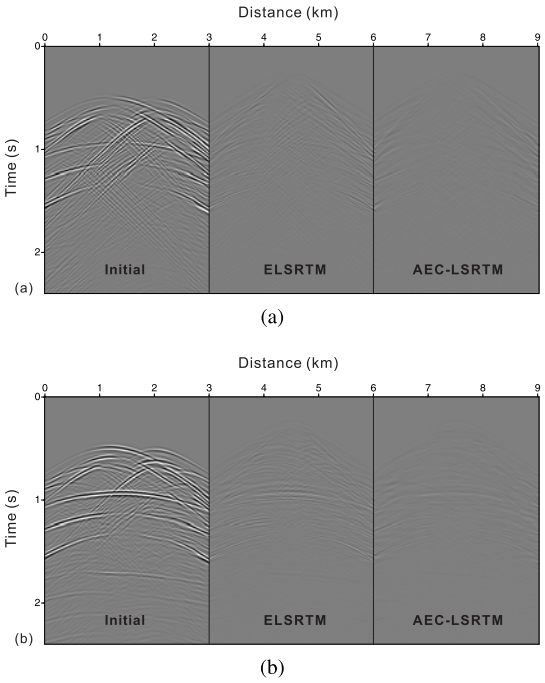

Fig. 7. Normalized single-shot data residuals of (a) u_x- and (b) u_z- components for the migration model, the AEC-LSRTM results, and the ELSRTM results.

3.2 s with a temporal sampling rate of 0.8 ms. Fig. 10 shows the observed multicomponent data, which contains a certain degree of Gaussian noise. The maximum iteration numbers of the LSM loop for the two methods are set to be 51.

Fig. 11 presents the migration images of Vp, Vs, and ρ using AEC-RTM. Although the first-arrivals have been removed in advance (marked by the black lines in Fig. 10), the obtained Vp and Vs images [Fig. 11(a) and (b)] still suffer from serious back-scatterings and unbalanced amplitude. Due to the high-contrast basement, the incident waves are

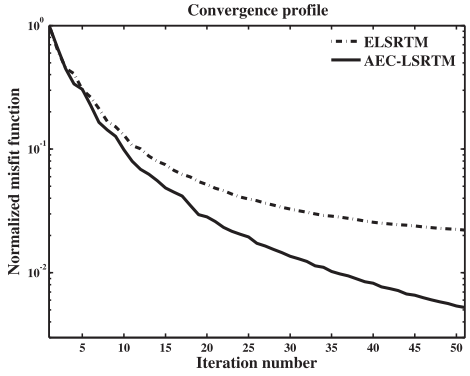

Fig. 8. Convergence profiles of AEC-LSRTM and ELSRTM. The values of misfit function have been normalized. The dashed line indicates the ELSRTM result, and the solid one denotes the AEC-LSRTM result.

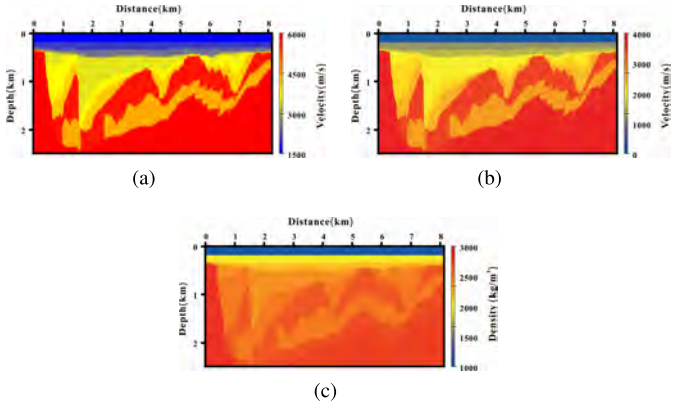

Fig. 9. True models of (a) Vp, (b) Vs, and (c) ρ.

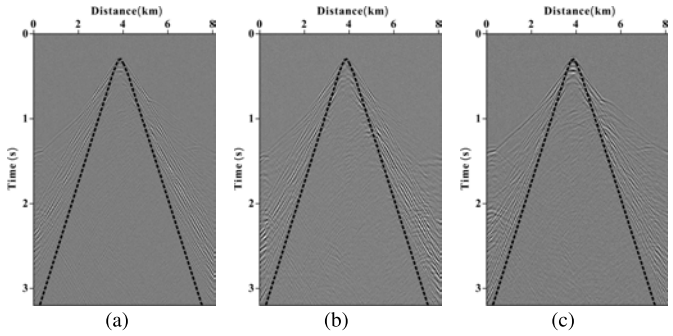

Fig. 10. Single-shot observed noisy data (SNR = 20) of (a) p-, (b) u_x-, and (c) u_z-components. First arrivals before the black lines are removed for migration. (a) p-wavefield. (b) u_x-wavefield. (c) u_z-wavefield.

mostly reflected at the depth of 0.4 km. As a consequence, the underlying structures cannot be well inverted. In contrast, the ρ image [Fig. 11(c)] is much better, showing high amplitude consistency and clear structures. It suggests that the density image can effectively mitigate those low-wavenumber noises and improve the imaging resolution. It is consistent with the sensitivity analysis that the ρ perturbation is more sensitive to reflections but has less sensitivity on transmission waves [43].

Fig. 12 presents the final LSM images of Vp, Vs, and ρ using ELSRTM and AEC-LSRTM. The ELSRTM images are

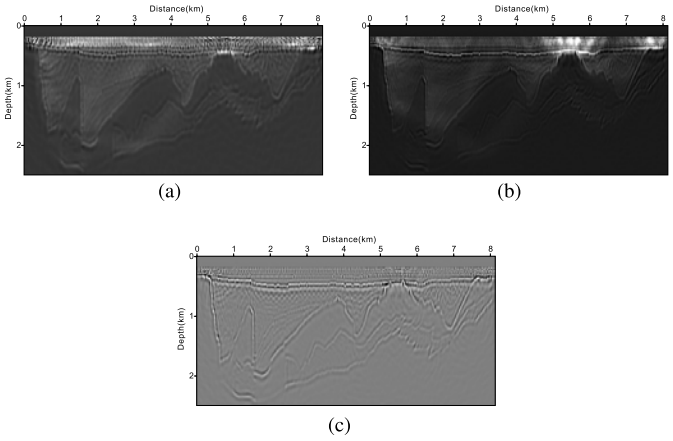

Fig. 11. Migration images of (a) Vp, (b) Vs, and (c) ρ using AEC-RTM.

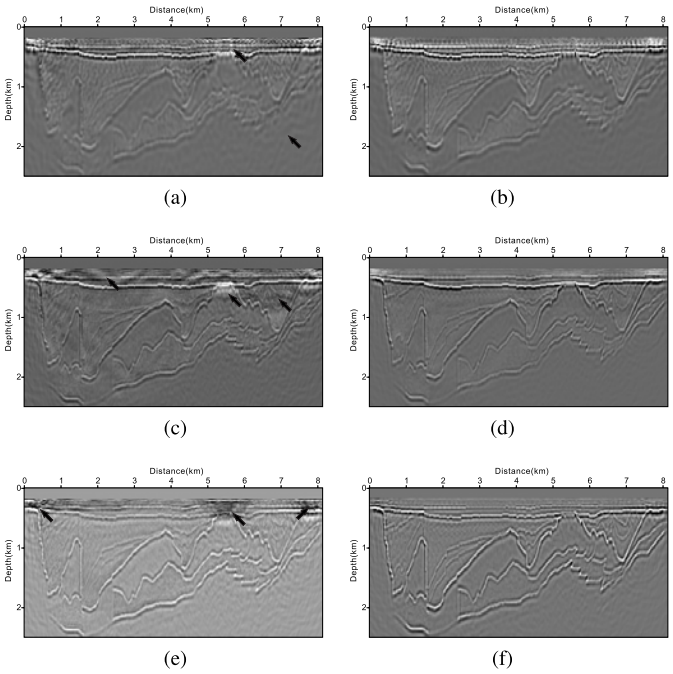

Fig. 12. Final LSM images using the (Left) ELSRTM and (Right) AEC-LSRTM methods of (a) and (b) Vp, (c) and (d) Vs, and (e) and (f) ρ. (a) Vp image using ELSRTM. (b) Vp image using AEC-LSRTM. (c) Vs image using ELSRTM. (d) Vs image using AEC-LSRTM. (e) ρ image using ELSRTM. (f) ρ image using AEC-LSRTM.

influenced by the backscattering energy (see arrows in Fig. 12) and the Gaussian noises from the observed data. On the contrary, the AEC-LSRTM method provides better-resolved structures with improved continuity and enhanced fidelity. The vertical profiles of elastic impedance reflectivity models are shown in Fig. 13. The AEC-LSRTM results are much closer to the true reflectivity model and give more accurate characterizations of the high-wavenumber reflecting interfaces.

IV. Discussion

In the previous section, we have validated the effectiveness of the AEC-LSRTM method for OBS 4C data. Due to the high acquisition costs, a typical ocean-bottom node (OBN)

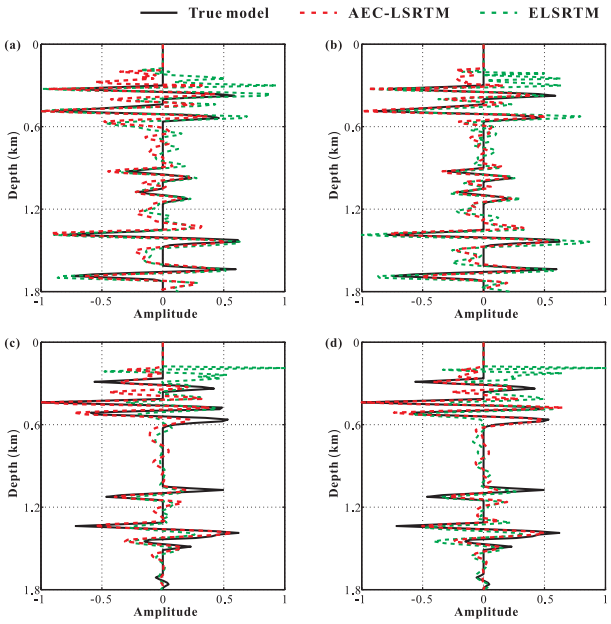

Fig. 13. Vertical profiles of (a) and (c) *P*- and (b) and (d) *S*-wave impedance reflectivity models at the distances of (Top) 2.5 km and (Bottom) 5.5 km.

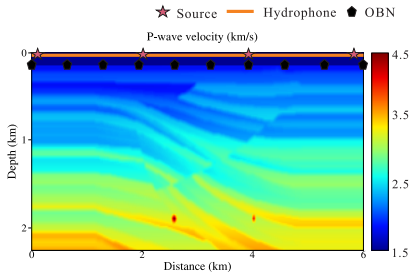

Fig. 14. True P-wave velocity model for the Sigbee2A model test. The sources and hydrophones are located below the sea surface, and the OBNs are placed on the seabed.

observation geometry may include only a few dozens of 4C receivers. As a consequence, limited observation apertures and sparse sampling intervals can significantly reduce the imaging quality. Fortunately, high-dense towed-streamer data acquired in the same exploration areas may be a useful supplement to the sparse OBN observation. This section investigates whether the AEC-LSRTM method can jointly migrate 1C towed-streamer data and 4C OBN data to obtain high-quality subsurface images.

Fig. 14 shows the true Vp of the Sigbee2A model. The S-wave velocity and density models below the seabed are built using the following formulas:

$$\begin{aligned} Vs(x,z) &= Vp(x,z)/1.5 \\ \rho(x,z) &= 310 \cdot Vp(x,z)^{0.25}. \end{aligned} \tag{13}$$

The migration models are generated using a Gaussian smoothing function with a window of 60 m. The acquisition geometries of OBN and hybrid observations are shown in Table II. The maximum iteration number of the LSM loop is 51.

Figs. 15 and 16 display the migration and LSM images, respectively. For the OBN observation, the obtained structures are not well retrieved, showing significant acquisition footprints (marked by arrows) and discontinuous reflecting events (marked by the ellipse). Although the footprints have been mostly eliminated by performing the LSM

TABLE II
ACQUISITION GEOMETRIES FOR OBN AND HYBRID OBSERVATIONS

	OBN	Hybrid
4C OBN	10	10
1C Hydrophone	0	400
P-wave Source	40	40

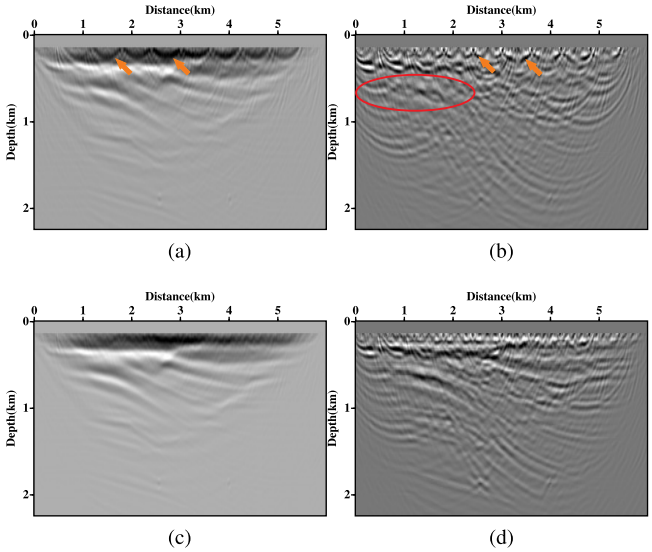

Fig. 15. Migration images for (Top) OBN and (Bottom) hybrid data. (a) Vp image with OBN data. (b) Vs image with OBN data. (c) Vp image with hyrid data. (d) Vs image with hyrid data.

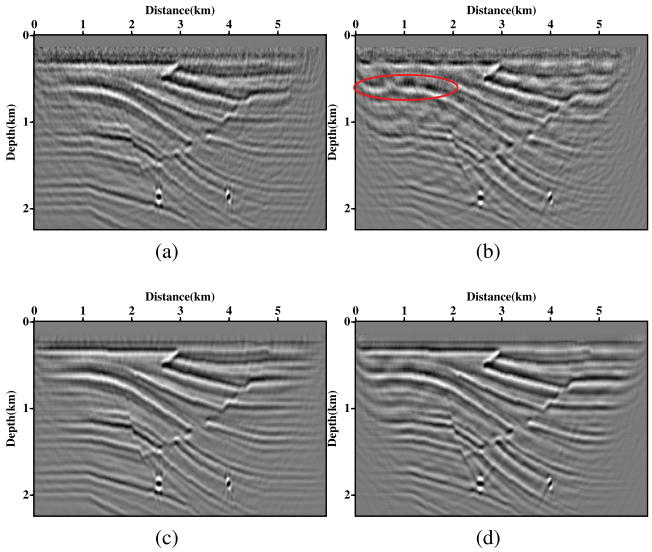

Fig. 16. LSM images for (Top) OBN and (Bottom) hybrid data. (a) Vp image with OBN data. (b) Vs image with OBN data. (c) Vp image with hyrid data. (d) Vs image with hyrid data.

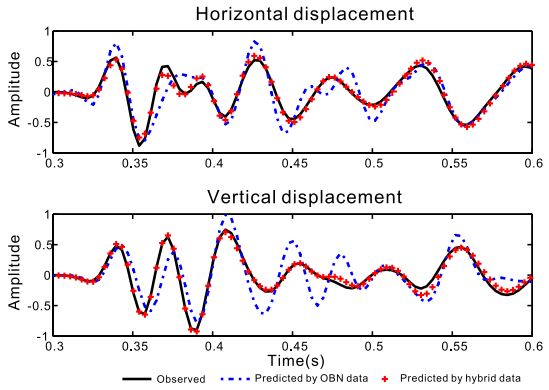

Fig. 17. Comparison of u_x- and u_z-component records of observed (black lines) and predicted using OBN (blue lines) and hybrid (red lines) data.

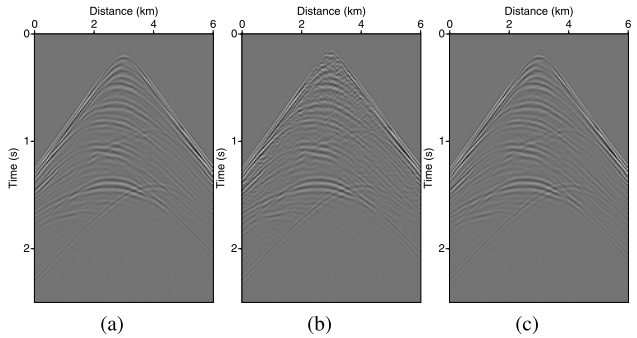

Fig. 18. Single-shot gathers of p-component data of observed (a) and predicted using (b) OBN and (c) hybrid data.

algorithm [see Fig. 16(a) and (b)], the reflecting layers are still distorted. As the marine towed-streamer data are simultaneously migrated, the footprints are mostly eliminated, providing less migration artifacts and better continuity [see Fig. 16(c) and (d)]. Figs. 17 and 18 present the predicted multicomponent records using the two observations. It shows that the records predicted by the OBN data have biased phases and inaccurate amplitude. In contrast, the results using the hybrid observation match the observed data more closely. The results suggest that the AEC-LSRTM method is useful to jointly migrate these two types of marine seismic data and suppress the acquisition footprints.

V. Conclusion

In this article, we have proposed a new ELSRTM method based on a modified acoustic-elastic coupled equation. Owing to the modified AEC equation, OBS 4C data can be predicted/migrated using a one-time wavefield simulation. The proposed method can yield multiple images and give quantitative estimations of subsurface impedance reflectivity at similar computational consumption as the conventional 3C ELSRTM method. Numerical experiments on the uncorrelated layer model and the Southern Yellow Sea model have validated that the method can enhance amplitude fidelity, improve spatial resolution, and suppress migration artifacts. The discussion shows that the AEC-LSRTM method can jointly utilize dense towed-streamer data to suppress the acquisition footprints caused by the sparse OBN observations. Of course, since the current AEC-LSRTM method is built on a waveform-based misfit function, it still suffers from the cycle-skipping problem when the migration models are not precise enough. In the future, we will make more use of the kinematic information of observed data to improve the stability and applicability of the algorithm.

Appendix A
Derivation of the Modified Acoustic-Elastic Coupled Equation

We start from the standard 2-D time-domain displacement-stress elastic wave equation, given by

$$\begin{cases} \rho\dfrac{\partial^2 u_x}{\partial t^2} = \dfrac{\partial \tau_{xx}}{\partial x} + \dfrac{\partial \tau_{xz}}{\partial z} \\ \rho\dfrac{\partial^2 u_z}{\partial t^2} = \dfrac{\partial \tau_{xz}}{\partial x} + \dfrac{\partial \tau_{zz}}{\partial z} \\ \tau_{xx} = (\lambda+2\mu)\dfrac{\partial u_x}{\partial x} + \lambda\dfrac{\partial u_z}{\partial z} + f \\ \tau_{zz} = (\lambda+2\mu)\dfrac{\partial u_z}{\partial z} + \lambda\dfrac{\partial u_x}{\partial x} + f \\ \tau_{xz} = \mu\left(\dfrac{\partial u_x}{\partial z} + \dfrac{\partial u_z}{\partial x}\right) \end{cases} \tag{A.1}$$

where u_x and u_z denote the horizontal- and vertical-particle displacement components, τ_{xx} and τ_{zz} are the normal stress components, and τ_{xz} is the shear stress component. λ and μ are the Lamé constants, and ρ is density. The source function f is implemented in τ_{xx} and τ_{zz} to generate a pure P-wave.

In the tensor analysis, the stress tensor $\mathbf{T}$ can be decomposed into the isotropic pressure $-p\mathbf{I}$ and the deviatoric $\boldsymbol{\tau}^s$ parts

$$\mathbf{T} = \boldsymbol{\tau}^s - p\mathbf{I} \tag{A.2}$$

where $\mathbf{I}$ is the identity matrix. It satisfies for 2-D case

$$\begin{aligned} p &= -\frac{1}{2}tr(\mathbf{T}) \\ &= -\frac{1}{2}(\tau_{xx}+\tau_{zz}) = -(\lambda+\mu)\left(\frac{\partial u_x}{\partial x} + \frac{\partial u_z}{\partial z}\right). \end{aligned} \tag{A.3}$$

As a result, the deviatoric stress components become

$$\begin{cases} \tau^s_{xx} = \tau_{xx} + p = \mu\dfrac{\partial u_x}{\partial x} - \mu\dfrac{\partial u_z}{\partial z} \\ \tau^s_{zz} = \tau_{zz} + p = \mu\dfrac{\partial u_z}{\partial z} - \mu\dfrac{\partial u_x}{\partial x} \\ \tau^s_{xz} = \tau_{xz} = \mu\dfrac{\partial u_x}{\partial z} + \mu\dfrac{\partial u_z}{\partial x}. \end{cases} \tag{A.4}$$

Substituting (A.4) into (A.1), we can obtain the original acoustic-elastic coupled equation referred to [39].

The original AEC equation includes six formulas, which is redundant in computing the pressure component. In this study, the stress components are defined as

$$\tau^s_n = \tau^s_{xx} = -\tau^s_{zz}, \quad \tau^s_s = \tau^s_{xz} \tag{A.5}$$

where τ_n^s and τ_s^s are the re-defined normal and deviatoric stress components. The modified AEC equation become

$$\begin{cases} \rho\dfrac{\partial^2 u_x}{\partial t^2} = \dfrac{\partial\left(\tau_n^s - p\right)}{\partial x} + \dfrac{\partial \tau_s^s}{\partial z} \\ \rho\dfrac{\partial^2 u_z}{\partial t^2} = \dfrac{\partial \tau_s^s}{\partial x} + \dfrac{\partial\left(-\tau_n^s - p\right)}{\partial z} = 0 \\ p = -(\lambda+\mu)\left(\dfrac{\partial u_x}{\partial x} + \dfrac{\partial u_z}{\partial z}\right) \\ \tau_n^s = \mu\left(\dfrac{\partial u_x}{\partial x} - \dfrac{\partial u_z}{\partial z}\right) \\ \tau_s^s = \mu\left(\dfrac{\partial u_x}{\partial z} + \dfrac{\partial u_z}{\partial x}\right). \end{cases} \tag{A.6}$$

As same as the original AEC equation, this one can also simulate the subsurface 4C seismic wavefields but it has advantages of decreasing the number of partial derivative equations and saving memory.

For completeness purpose, we also derive the modified AEC equation in 3-D. The 3-D original AEC equation is given by

$$\begin{cases} \rho\dfrac{\partial^2 u_x}{\partial t^2} = \dfrac{\partial(\tau_{xx}^s - p)}{\partial x} + \dfrac{\partial \tau_{xy}^s}{\partial y} + \dfrac{\partial \tau_{xz}^s}{\partial z} \\ \rho\dfrac{\partial^2 u_y}{\partial t^2} = \dfrac{\partial \tau_{xy}^s}{\partial x} + \dfrac{\partial(\tau_{yy}^s - p)}{\partial y} + \dfrac{\partial \tau_{yz}^s}{\partial z} \\ \rho\dfrac{\partial^2 u_z}{\partial t^2} = \dfrac{\partial \tau_{xz}^s}{\partial x} + \dfrac{\partial \tau_{yz}^s}{\partial y} + \dfrac{\partial(\tau_{zz}^s - p)}{\partial z} \end{cases} \tag{A.7}$$

and

$$\begin{cases} p = -\left(\lambda + \dfrac{2}{3}\mu\right)\left(\dfrac{\partial u_x}{\partial x} + \dfrac{\partial u_y}{\partial y} + \dfrac{\partial u_z}{\partial z}\right) \\ \tau_{xx}^s = \dfrac{2}{3}\mu\left(2\dfrac{\partial u_x}{\partial x} - \dfrac{\partial u_y}{\partial y} - \dfrac{\partial u_z}{\partial z}\right) \\ \tau_{yy}^s = \dfrac{2}{3}\mu\left(2\dfrac{\partial u_y}{\partial y} - \dfrac{\partial u_x}{\partial x} - \dfrac{\partial u_z}{\partial z}\right) \\ \tau_{zz}^s = \dfrac{2}{3}\mu\left(2\dfrac{\partial u_z}{\partial z} - \dfrac{\partial u_x}{\partial x} - \dfrac{\partial u_y}{\partial y}\right) \\ \tau_{xz}^s = \mu\left(\dfrac{\partial u_x}{\partial z} + \dfrac{\partial u_z}{\partial x}\right) \\ \tau_{xy}^s = \mu\left(\dfrac{\partial u_x}{\partial y} + \dfrac{\partial u_y}{\partial x}\right) \\ \tau_{yz}^s = \mu\left(\dfrac{\partial u_y}{\partial z} + \dfrac{\partial u_z}{\partial y}\right). \end{cases} \tag{A.8}$$

Because $\tau_{xx}^s + \tau_{yy}^s + \tau_{zz}^s = 0$, we can similarly provide a 3-D modified AEC equation by replacing τ_{yy}^s as $-(\tau_{xx}^s + \tau_{zz}^s)$ to reduce the number of formulas.

Appendix B
Derivation of Adjoint Equation and Gradient for the AEC-LSRTM Method

The modified AEC equation can be rewritten as

$$\mathbf{S}\mathbf{w} = \mathbf{f} \tag{B.1}$$

where $\mathbf{w} = \left(u_x, u_z, p, \tau_n^s, \tau_s^s\right)^T$ denotes the elastic wavefields, $\mathbf{f} = \left(0, 0, f_p, 0, 0\right)^T$ indicates the source wavelet and $\mathbf{S}$ is the parameter derivative matrix

$$\mathbf{S} = \begin{pmatrix} \rho\dfrac{\partial^2}{\partial t^2} & 0 & \dfrac{\partial}{\partial x} & -\dfrac{\partial}{\partial x} & -\dfrac{\partial}{\partial z} \\ 0 & \rho\dfrac{\partial^2}{\partial t^2} & \dfrac{\partial}{\partial z} & \dfrac{\partial}{\partial z} & -\dfrac{\partial}{\partial x} \\ (\lambda+\mu)\dfrac{\partial}{\partial x} & (\lambda+\mu)\dfrac{\partial}{\partial z} & 1 & 0 & 0 \\ -\mu\dfrac{\partial}{\partial x} & \mu\dfrac{\partial}{\partial z} & 0 & 1 & 0 \\ -\mu\dfrac{\partial}{\partial z} & -\mu\dfrac{\partial}{\partial x} & 0 & 0 & 1 \end{pmatrix}. \tag{B.2}$$

Based on the perturbation imaging condition, the migration image is equivalent with the gradient of the misfit function (4)

$$\frac{\partial E}{\partial \mathbf{m}} = \left(\frac{\partial d_x}{\partial \mathbf{m}}\right)^T \cdot f'_x + \left(\frac{\partial d_z}{\partial \mathbf{m}}\right)^T \cdot f'_z + \left(\frac{\partial d_p}{\partial \mathbf{m}}\right)^T \cdot f'_p \tag{B.3}$$

where $\partial\mathbf{d}/\partial\mathbf{m}$ is the first-order partial derivative of elastic wavefield (at the receiver position) with respective to parameters, and $\mathbf{f}$ is the multicomponent adjoint source, satisfying

$$\begin{bmatrix} f'_x \\ f'_z \\ f'_p \end{bmatrix} = \begin{bmatrix} \varepsilon \cdot \delta d_x \\ \varepsilon \cdot \delta d_z \\ (1-\varepsilon)\cdot\zeta\cdot\delta d_p \end{bmatrix}. \tag{B.4}$$

Taking the derivative of (B.1), we have

$$\frac{\partial \mathbf{S}}{\partial \mathbf{m}}\mathbf{w} + \mathbf{S}\frac{\partial \mathbf{w}}{\partial \mathbf{m}} = 0 \tag{B.5}$$

and

$$\mathbf{L} = \frac{\partial \mathbf{w}}{\partial \mathbf{m}} = -\left(\mathbf{S}^{-1}\right)\frac{\partial \mathbf{S}}{\partial \mathbf{m}}\mathbf{w}. \tag{B.6}$$

Substituting (B.6) into (B.3), the gradient can be rewritten as

$$\frac{\partial E}{\partial \mathbf{m}} = \left[-\left(\mathbf{S}^{-1}\right)\frac{\partial \mathbf{S}}{\partial \mathbf{m}}\mathbf{w}\right]^T \mathbf{f}' \tag{B.7}$$

and

$$\frac{\partial E}{\partial \mathbf{m}} = -\left[\frac{\partial \mathbf{S}}{\partial \mathbf{m}}\mathbf{w}\right]^T \left(\mathbf{S}^T\right)^{-1}\mathbf{f}'. \tag{B.8}$$

Here $\mathbf{S}^T$ is the adjoint operator of the modified AEC-equation, given by

$$\mathbf{S}^T = \begin{pmatrix} \rho\dfrac{\partial^2}{\partial t^2} & 0 & -\dfrac{\partial}{\partial x}(\lambda+\mu) & \dfrac{\partial}{\partial x}\mu & \dfrac{\partial}{\partial z}\mu \\ 0 & \rho\dfrac{\partial^2}{\partial t^2} & -\dfrac{\partial}{\partial z}(\lambda+\mu) & -\dfrac{\partial}{\partial z}\mu & \dfrac{\partial}{\partial x}\mu \\ -\dfrac{\partial}{\partial x} & -\dfrac{\partial}{\partial z} & 1 & 0 & 0 \\ \dfrac{\partial}{\partial x} & -\dfrac{\partial}{\partial z} & 0 & 1 & 0 \\ \dfrac{\partial}{\partial z} & \dfrac{\partial}{\partial x} & 0 & 0 & 1 \end{pmatrix}. \tag{B.9}$$

According to the adjoint-state theory, we define $\hat{\mathbf{w}} = \left(\mathbf{S}^{-1}\right)^T\mathbf{f}'$ as the solution of the adjoint equation

$$\mathbf{S}^T\hat{\mathbf{w}} = \mathbf{f}' \tag{B.10}$$

where $\hat{\mathbf{w}} = \left(\hat{u}_x, \hat{u}_z, \hat{p}, \hat{\tau}_n^s, \hat{\tau}_s^s\right)^T$ is the adjoint variables.

For the parameterization of Lamé constants and density $\mathbf{m} = [\lambda, \mu, \rho]^T$, the partial derivative matrices can be given by

$$\frac{\partial \mathbf{S}}{\partial \lambda} = \begin{pmatrix} 0 & 0 & 0 & 0 & 0 \\ 0 & 0 & 0 & 0 & 0 \\ \dfrac{\partial}{\partial x} & \dfrac{\partial}{\partial z} & 0 & 0 & 0 \\ 0 & 0 & 0 & 0 & 0 \\ 0 & 0 & 0 & 0 & 0 \end{pmatrix} \tag{B.11}$$

$$\frac{\partial \mathbf{S}}{\partial \mu} = \begin{pmatrix} 0 & 0 & 0 & 0 & 0 \\ 0 & 0 & 0 & 0 & 0 \\ \dfrac{\partial}{\partial x} & \dfrac{\partial}{\partial z} & 0 & 0 & 0 \\ -\dfrac{\partial}{\partial x} & \dfrac{\partial}{\partial z} & 0 & 0 & 0 \\ -\dfrac{\partial}{\partial z} & -\dfrac{\partial}{\partial x} & 0 & 0 & 0 \end{pmatrix} \tag{B.12}$$

and

$$\frac{\partial \mathbf{S}}{\partial \rho} = \begin{pmatrix} \dfrac{\partial^2}{\partial t^2} & 0 & 0 & 0 & 0 \\ 0 & \dfrac{\partial^2}{\partial t^2} & 0 & 0 & 0 \\ 0 & 0 & 0 & 0 & 0 \\ 0 & 0 & 0 & 0 & 0 \\ 0 & 0 & 0 & 0 & 0 \end{pmatrix}. \tag{B.13}$$

Substituting equations (B.10)–(B.13) into (B.8), the gradients of the Lamé constants and density can be given by

$$\begin{cases} \dfrac{\partial E}{\partial \lambda} = -\dfrac{p}{\lambda+\mu}\hat{p} \\ \dfrac{\partial E}{\partial \mu} = -\dfrac{p}{\lambda+\mu}\hat{p} - \dfrac{\tau_n^s}{\mu}\hat{\tau}_n^s - \dfrac{\tau_s^s}{\mu}\hat{\tau}_s^s \\ \dfrac{\partial E}{\partial \rho} = \dfrac{\partial^2 u_x}{\partial t^2}\hat{u}_x + \dfrac{\partial^2 u_z}{\partial t^2}\hat{u}_z. \end{cases} \tag{B.14}$$

Appendix C
Derivation of Multiparameter Diagonal Hessian for Modified AEC Equation

As defined in (10), the Hessian operator for LSM can be given by

$$\mathbf{H} = \mathbf{L}^T\mathbf{L}. \tag{C.1}$$

Substituting (B.6) into (C.1), we can get

$$\mathbf{H} = \left(\frac{\partial \mathbf{S}}{\partial \mathbf{m}}\mathbf{w}\cdot\mathbf{S}^{-1}\right)^T\left(\frac{\partial \mathbf{S}}{\partial \mathbf{m}}\mathbf{w}\cdot\mathbf{S}^{-1}\right). \tag{C.2}$$

Here, $\mathbf{S}^{-1}$ denotes the elastodynamic Green's function from each receiver, which requires a large amount of computational cost. In this article, we use a diagonal pseudo-Hessian operator [44]

$$\mathbf{H}_d = \left(\frac{\partial \mathbf{S}}{\partial \mathbf{m}}\mathbf{w}\right)^T\left(\frac{\partial \mathbf{S}}{\partial \mathbf{m}}\mathbf{w}\right). \tag{C.3}$$

The diagonal blocks of the Hessian for Lamé constants and density can be given by

$$\begin{cases} H_{\lambda\lambda} = \left(\dfrac{\partial \mathbf{S}}{\partial \lambda}\mathbf{w}\right)^T\left(\dfrac{\partial \mathbf{S}}{\partial \lambda}\mathbf{w}\right) = \left(\dfrac{p}{\lambda+\mu}\right)^2 \\ H_{\mu\mu} = \left(\dfrac{\partial \mathbf{S}}{\partial \mu}\mathbf{w}\right)^T\left(\dfrac{\partial \mathbf{S}}{\partial \mu}\mathbf{w}\right) = \left(\dfrac{p}{\lambda+\mu}\right)^2 + \left(\dfrac{\tau_n^s}{\mu}\right)^2 + \left(\dfrac{\tau_s^s}{\mu}\right)^2 \\ H_{\rho\rho} = \left(\dfrac{\partial \mathbf{S}}{\partial \rho}\mathbf{w}\right)^T\left(\dfrac{\partial \mathbf{S}}{\partial \rho}\mathbf{w}\right) = \dfrac{\partial^2 u_x}{\partial t^2}\dfrac{\partial^2 u_x}{\partial t^2} + \dfrac{\partial^2 u_z}{\partial t^2}\dfrac{\partial^2 u_z}{\partial t^2}. \end{cases} \tag{C.4}$$

Then, the diagonal blocks of Hessian for P- and S-wave velocities and density can be obtained via the chain law (9)

$$\begin{aligned} &\begin{bmatrix} H_{VpVp} & 0 & 0 \\ 0 & H_{VsVs} & 0 \\ 0 & 0 & H_{\rho\rho} \end{bmatrix} \\ &= \begin{bmatrix} 2\rho & 0 & 0 \\ -4Vs\rho & 2Vs\rho & 0 \\ Vp^2 - 2Vs^2 & Vs^2 & 1 \end{bmatrix} \cdot \begin{bmatrix} H_{\lambda\lambda} & 0 & 0 \\ 0 & H_{\mu\mu} & 0 \\ 0 & 0 & H_{\rho\rho} \end{bmatrix} \\ &\quad \cdot \begin{bmatrix} 2\rho & 0 & 0 \\ -4Vs\rho & 2Vs\rho & 0 \\ Vp^2 - 2Vs^2 & Vs^2 & 1 \end{bmatrix}^T \end{aligned} \tag{C.5}$$

and we have

$$\begin{cases} H_{VpVp} = 4Vp^2\rho^2 H_{\lambda\lambda} \\ H_{VsVs} = 16Vs^2\rho^2 H_{\lambda\lambda} + 4Vs^2\rho^2 H_{\mu\mu} + H_{\rho\rho} \\ H_{\rho\rho} = \left(Vp^2 - 2Vs^2\right)^2 H_{\lambda\lambda} + Vs^4 H_{\mu\mu} + H_{\rho\rho}. \end{cases} \tag{C.6}$$

References

[1] E. Baysal, D. D. Kosloff, and J. W. Sherwood, "Reverse time migration," *Geophysics*, vol. 48, no. 11, pp. 1514–1524, 1983.

[2] G. A. McMECHAN, "Migration by extrapolation of time-dependent boundary values," *Geophys. Prospecting*, vol. 31, no. 3, pp. 413–420, Jun. 1983.

[3] T. Nemeth, C. Wu, and G. T. Schuster, "Least-squares migration of incomplete reflection data," *Geophysics*, vol. 64, no. 1, pp. 208–221, Jan. 1999.

[4] G. T. Schuster, "Least-squares cross-well migration," in *Proc. SEG Tech. Program Expanded Abstr.*, Jan. 1993, pp. 110–113.

[5] Y. Tang, "Target-oriented wave-equation least-squares migration/inversion with phase-encoded hessian," *Geophysics*, vol. 74, no. 6, pp. WCA95–WCA107, Nov. 2009.

[6] W. Dai, X. Wang, and G. T. Schuster, "Least-squares migration of multisource data with a deblurring filter," *Geophysics*, vol. 76, no. 5, pp. R135–R146, Sep. 2011.

[7] M. Wong, S. Ronen, and B. Biondi, "Least-squares reverse time migration/inversion for ocean bottom data: A case study," in *Proc. SEG Tech. Program Expanded Abstr.*, Jan. 2011, pp. 2369–2373.

[8] Y. Liu, J. Yang, B. Chi, and L. Dong, "An improved scattering-integral approach for frequency-domain full waveform inversion," *Geophys. J. Int.*, vol. 202, no. 3, pp. 1827–1842, Sep. 2015.

[9] Y. Zhang, L. Duan, and Y. Xie, "A stable and practical implementation of least-squares reverse time migration," *Geophysics*, vol. 80, no. 1, pp. V23–V31, Jan. 2015.

[10] D. Wu, G. Yao, J. Cao, and Y. Wang, "Least-squares RTM with l1 norm regularisation," *J. Geophys. Eng.*, vol. 13, no. 5, pp. 666–673, Oct. 2016.

[11] G. Yao and H. Jakubowicz, "Least-squares reverse-time migration in a matrix-based formulation," *Geophys. Prospecting*, vol. 64, no. 3, pp. 611–621, May 2016.

[12] X. Fang, F. Niu, and D. Wu, "Least-squares reverse-time migration enhanced with the inverse scattering imaging condition," *Chin. J. Geophys.*, vol. 61, no. 9, pp. 3770–3782, 2018.

[13] D. Rocha, P. Sava, and A. Guitton, "3D acoustic least-squares reverse time migration using the energy norm," *Geophysics*, vol. 83, no. 3, pp. S261–S270, May 2018.

[14] G. Dutta and G. T. Schuster, "Attenuation compensation for least-squares reverse time migration using the viscoacoustic-wave equation," *Geophysics*, vol. 79, no. 6, pp. S251–S262, Nov. 2014.
[15] J. Yang, Y. Liu, and L. Dong, "Least-squares reverse time migration in the presence of density variations," *Geophysics*, vol. 81, no. 6, pp. S497–S509, Nov. 2016.
[16] J. Yang, Y. Liu, Y. E. Li, A. Cheng, L. Dong, and Y. Du, "Joint least-squares reverse time migration of primary and prismatic waves," *Geophysics*, vol. 84, no. 1, pp. S29–S40, Jan. 2019.
[17] T. J. Sears, P. J. Barton, and S. C. Singh, "Elastic full waveform inversion of multicomponent ocean-bottom cable seismic data: Application to alba field, U. K. North Sea," *Geophysics*, vol. 75, no. 6, pp. R109–R119, Nov. 2010.
[18] W.-F. Chang and G. A. McMechan, "Elastic reverse-time migration," *Geophysics*, vol. 52, no. 10, pp. 1365–1375, 1987.
[19] J. Yan and P. Sava, "Isotropic angle-domain elastic reverse-time migration," *Geophysics*, vol. 73, no. 6, pp. S229–S239, Nov. 2008.
[20] Y. Duan and P. Sava, "Scalar imaging condition for elastic reverse time migration," *Geophysics*, vol. 80, no. 4, pp. S127–S136, Jul. 2015.
[21] W. Wang and G. A. McMechan, "Vector-based elastic reverse time migrationvector-based elastic RTM," *Geophysics*, vol. 80, no. 6, pp. S245–S258, 2015.
[22] R. R. Stewart, J. E. Gaiser, R. J. Brown, and D. C. Lawton, "Converted-wave seismic exploration: Applications," *Geophysics*, vol. 68, no. 1, pp. 40–57, 2003.
[23] A. Stanton and M. Sacchi, "Least squares wave equation migration of elastic data," in *Proc. 77th EAGE Conf. Exhib.*, Jun. 2015, pp. 1–5.
[24] A. Stanton and M. D. Sacchi, "Elastic least-squares one-way wave-equation migration," *Geophysics*, vol. 82, no. 4, pp. S293–S305, Jul. 2017.
[25] Y. Duan, A. Guitton, and P. Sava, "Elastic least-squares reverse time migration," *Geophysics*, vol. 82, no. 4, pp. S315–S325, Jul. 2017.
[26] Z. Feng and G. T. Schuster, "Elastic least-squares reverse time migration," *Geophysics*, vol. 82, no. 2, pp. S143–S157, 2017.
[27] Q. Guo and T. Alkhalifah, "Elastic reflection-based waveform inversion with a nonlinear approach," *Geophysics*, vol. 82, no. 6, pp. R309–R321, Nov. 2017.
[28] Z. Ren, Y. Liu, and M. K. Sen, "Least-squares reverse time migration in elastic media," *Geophys. J. Int.*, vol. 208, no. 2, pp. 1103–1125, 2017.
[29] M. Sun, L. Dong, J. Yang, C. Huang, and Y. Liu, "Elastic least-squares reverse time migration with density variations," *Geophysics*, vol. 83, no. 6, pp. S533–S547, Nov. 2018.
[30] Y. Qu, J. Li, J. Huang, and Z. Li, "Elastic least-squares reverse time migration with velocities and density perturbation," *Geophys. J. Int.*, vol. 212, no. 2, pp. 1033–1056, Feb. 2018.
[31] J. Zhang, "Wave propagation across fluid-solid interfaces: A grid method approach," *Geophys. J. Int.*, vol. 159, no. 1, pp. 240–252, Oct. 2004.
[32] Y. Choi, D.-J. Min, and C. Shin, "Two-dimensional waveform inversion of multi-component data in acoustic-elastic coupled media," *Geophys. Prospecting*, vol. 56, no. 6, pp. 863–881, Nov. 2008.
[33] H. Singh, J. Shragge, and I. Tsvankin, "Coupled-domain acoustic-elastic solver for anisotropic media: A mimetic finite difference approach," SEG Tech. Program Expanded Abstr., Tech. Rep., 2019, pp. 3755–3759.
[34] Y. Qu, Z. Guan, J. Li, and Z. Li, "Fluid-solid coupled full-waveform inversion in the curvilinear coordinates for ocean-bottom cable data," *Geophysics*, vol. 85, no. 3, pp. R113–R133, May 2020.
[35] J. D. De Basabe and M. K. Sen, "A comparison of monolithic methods for elastic wave propagation in media with a fluid–solid interface," in *Proc. SEG Tech. Program. Expanded Abstr.*, 2014, pp. 3323–3328.
[36] Y. Qu, J. Huang, Z. Li, and J. Li, "A hybrid grid method in an auxiliary coordinate system for irregular fluid–solid interface modelling," *Geophys. J. Int.*, vol. 208, no. 3, pp. 1540–1556, Mar. 2017.
[37] Y.-C. Sun, W. Zhang, J.-K. Xu, and X. Chen, "Numerical simulation of 2-D seismic wave propagation in the presence of a topographic fluid–solid interface at the sea bottom by the curvilinear grid finite-difference method," *Geophys. J. Int.*, vol. 210, no. 3, pp. 1721–1738, Sep. 2017.
[38] Y. Qu, C. Zhou, C. Liu, Z. Li, and J. Li, "P- and S-wave separated elastic reverse time migration for OBC data from fluid–solid coupled media with irregular seabed interfaces," *J. Appl. Geophys.*, vol. 172, Jan. 2020, Art. no. 103882.
[39] P. Yu, J. Geng, X. Li, and C. Wang, "Acoustic-elastic coupled equation for ocean bottom seismic data elastic reverse time migration," *Geophysics*, vol. 81, no. 5, pp. S333–S345, Sep. 2016.
[40] P. Yu, J. Geng, and J. Ma, "Vector-wave-based elastic reverse time migration of ocean-bottom 4C seismic data," *Geophysics*, vol. 83, no. 4, pp. S333–S343, Jul. 2018.
[41] P. Yu and J. Geng, "Acoustic-elastic coupled equations in vertical transverse isotropic media for pseudoacoustic-wave reverse time migration of ocean-bottom 4C seismic data," *Geophysics*, vol. 84, no. 4, pp. S317–S327, Jul. 2019.
[42] J. Virieux, "P-SV wave propagation in heterogeneous media: Velocity-stress finite-difference method," *Geophysics*, vol. 51, no. 4, pp. 889–901, 1986.
[43] M. Sun, J. Yang, L. Dong, Y. Liu, and C. Huang, "Density reconstruction in multiparameter elastic full-waveform inversion," *J. Geophys. Eng.*, vol. 14, no. 6, pp. 1445–1462, Dec. 2017.
[44] C. Shin, S. Jang, and D.-J. Min, "Improved amplitude preservation for prestack depth migration by inverse scattering theory," *Geophys. Prospecting*, vol. 49, no. 5, pp. 592–606, Sep. 2001.

Minao Sun was born in Anhui, China, in January 1990. He received the B.Sc. and Ph.D. degrees in geophysics from Tongji University, Shanghai, China, in 2012 and 2018, respectively.

He was a Post-Doctoral Researcher with the Nanjing University of information Science and Technology, Nanjing, China. He is now working with the Sinopec Geophysical Institute, Nanjing, China. His research interests include wave propagation and imaging in heterogeneous media, full waveform inversion, optimization method and parallel computing.

Shuanggen Jin was born in Anhui, China, in 1974. He received the B.Sc. degree in geodesy from Wuhan University, Wuhan, China, in 1999, and the Ph.D. degree in geodesy from the University of Chinese Academy of Sciences, Beijing, China, in 2003.

He is a Professor and the Dean of the School of Remote Sensing and Geomatics Engineering, Nanjing University of Information Science and Technology, Nanjing, China, and also a Professor with the Shanghai Astronomical Observatory, CAS, Shanghai, China. He has authored or coauthored more than 500 articles in peer-reviewed journals and proceedings, 10 patents/software copyrights, and 10 books/monographs with more than 7000 citations and over 45 H-index. His main research interests include satellite navigation, remote sensing, space geodesy, and space/planetary exploration.

Dr. Jin was a Fellow of IAG in 2011. He was a member of the Russian Academy of Natural Sciences in 2017, the European Academy of Sciences in 2018, the Academia Europaea in 2019, and the Turkish Academy of Sciences in 2020, and an IUGG Fellow in 2019. He has been an Editorial Board Member of GPS Solutions, since 2016, *Journal of Geodynamics*, since 2014, and *Planetary and Space Science*, since 2014. He has received 1 First Class and 4 Second-Class Prizes of Provincial Awards and the 100-Talent Program of CAS (2010). He also received the Fu Chengyi Youth Science and Technology Award, in 2012, and the Xia Jianbai Award of Geomatics in 2014. He was the President of the International Association of Planetary Sciences (IAPS), from 2013 to 2017, and the International Association of CPGPS, from 2016 to 2017, the Chair of the IUGG Union Commission on Planetary Sciences (UCPS), from 2015 to 2023, and the Vice-President of the IAG Commission 2, from 2015 to 2019, and the COSPAR's Panel on Satellite Dynamics (PSD) (2016–2020). He has been the Editor-in-Chief of the *International Journal of Geosciences*, since 2010, and an Associate Editor of the IEEE TRANSACTIONS ON GEOSCIENCE AND REMOTE SENSING, since 2014, and *The Journal of Navigation*, since 2014. He was an Associate Editor of *Advances in Space Research*, from 2013 to 2017.

Pengfei Yu (Member, IEEE) was born in Shandong, China, in May 1987. He received the B.Sc. degree in geophysics from the China University of mining and technology, Xuzhou, China, in 2009, and the Ph.D. degree in solid geophysics from Tongji University, Shanghai, China, in 2016.

He is a Lecturer with Hohai University, Nanjing, China. His research interests include marine seismic data processing, wave propagation in fluid–solid media, and elastic imaging of OBS/OBN 4C data.